Processing and Application of Ceramics 17 [2] (2023) 181–188
https://doi.org/10.2298/PAC2302181N

Study of phase evolution and dielectric properties of $Sr_2Mn_{0.7}Sn_{0.3}O_4$

Gurudeo Nirala, Shail Upadhyay*

Department of Physics, Indian Institute of Technology (BHU), Varanasi-221005, India

Received 8 September 2022; Received in revised form 3 May 2023; Accepted 15 June 2023

Abstract

Ruddlesden-Popper oxide $Sr_2Mn_{0.7}Sn_{0.3}O_4$ was synthesized by solid state method by calcining at different temperatures between 1200 and 1500 °C. The phase evolution during thermal treatments was investigated and it was shown that the powder calcined at 1500 °C and ceramics sintered at 1500 °C have single phase structure. Rietveld refinement of the XRD data confirmed tetragonal crystal structure having $a = b = 3.9425$ Å and $c = 12.1230$ Å lattice parameters and I4/mmm space group symmetry. Permittivity (ε), impedance (Z^*), dissipation factor ($\tan\delta$) and AC conductivity (σ_{AC}) of the samples were studied in the frequency range 1 kHz–2 MHz and temperature range 60–600 °C. An equivalent circuit comprising two parallel R-L elements and one constant phase element (CPE) model fitted the impedance data very well. Components of the equivalent circuit were correlated with compositional micro inhomogeneities in the sintered sample. Resonance-like feature observed in the dissipation factor at a particular temperature is attributed to the cancellation of capacitive and inductive reactants. Negative permittivity and loss of the sintered sample were compared with other ceramic oxides showing negative permittivity.

Keywords: *Ruddlesden-Popper oxides, solid state synthesis, phase evolution, dielectrics, negative permittivity*

I. Introduction

Common dielectrics have positive values of permittivity and are used for storage applications (as a capacitor). Recently, negative permittivity materials (metamaterials) have attracted attention in comparison to the conventional positive dielectric constant materials owing to the advances of metacomposites and their multifunctional applications. Materials showing negative permittivity became promising candidates for high-power microwave filters [1], coil-free electrical inductors [2], novel capacitors [3–5], electromagnetic shielding [6,7]. In metamaterials, the modulation of negative permittivity is often based on metal building blocks with a complexity controlled by their geometry and configurations [8,9]. Tuning of the negative permittivity by compositional and microstructural modifications is possible only in "natural" materials. To meet the requirement of natural materials with negative permittivity, ceramic matrix composites (CMC) [10–12] and polymer matrix composites (PMC) [13,14] were developed. However, in these metacomposites realization of negative permittivity at molecular and atomic level is not possible which hinders application of metacomposites in form of coatings, thin films and even lower-dimension systems [15,16]. To overcome this problem significant efforts have been made to discover and develop single-phase homogeneous materials showing negative permittivity. Thus, recently few single-phase ceramics, like $PrMnO_3$ and $La_{1-x}Sr_xMnO_3$, showing negative permittivity have been reported in the literature [17,18]. The negative permittivity in these ceramics is attributed to their metal-like characteristics. Negative permittivity of these ceramic oxides could be tuned by compositional modifications, temperature and frequency.

Compound Sr_2MnO_4 belongs to the Ruddlesden-Popper (RP) family which has chemical formula $A_{n+1}B_nX_{3n+1}$ and was for the first time synthesized and characterized by Baltz and Plieth [19]. They reported that Sr_2MnO_4 is iso-structural to K_2NiF_4 and its lattice parameters are $a = b = 3.79$ Å and $c = 12.438$ Å. Synthesis of pure Sr_2MnO_4 phase using conventional solid state method in ambient atmosphere is not possible. After a rigorous exercise of changing processing parameter (cooling rate) we had successfully synthesised a single phase Sr_2MnO_4 by quenching in air from 1500 °C [20].

Synthesis of ceramic oxides by quenching is not a practical approach because it induces thermal stress

*Corresponding authors: tel: +8860364525,
e-mail: *supadhyay.app@itbhu.ac.in*

which could be a threat to long-term stability. It was reported that partial replacement of Sr by La and Mn by Ti makes synthesis cost effective (by lowering temperature) and practical [21–23]. It was also reported that when amount of La in the $Sr_{2-x}La_xMnO_4$ system is $x \geq 0.25$ the single phase ceramics can be obtained [24]. In addition, it was shown that $La_{1-x}Sr_xMnO_4$ has negative permittivity which was attributed to their metal-like characteristics.

In this work our attempt was to synthesize single-phase $Sr_2Mn_{0.7}Sn_{0.3}O_4$ powder and corresponding ceramics. Selection of Sn^{4+} was made because difference in the ionic radii of dopant Sn^{4+} (0.69 Å) and host Mn^{4+} (0.53 Å) in six-fold coordination is, according to the Hume-Rothery rule, appropriate for the solid solution formation. Recently we carried out dielectric measurement at high temperature (RT–600 °C) of the compound Sr_2MnO_4 and found negative permittivity behaviour in Sr_2MnO_4. We observed that this compound shows negative dielectric constant but above 500 °C [25] and also in Nb substituted Sr_2MnO_4 [26]. Thus, in this work we study the effect of Sn doping on structure and electric/dielectric properties of Sr_2MnO_4 ceramics.

II. Experimental

Stoichiometric amounts of strontium oxide ($SrCO_3$) manganese oxide (MnO_2) and tin oxide (SnO_2), purchased from Alfa Aser, China with purity ≥99.9%, were ball milled (PM-200, Retsch, Germany) for 8 h using acetone as mixing medium. Thereafter, the mixture was calcined at 1200 °C for 12 h in a high-temperature furnace (HTRH-70/150, Carbolite Gero, UK). The resultant powder was ground and re-calcined at 1300 °C for 12 h; the same process was repeated at 1400 and 1500 °C. The obtained powders were uniaxially pressed with a hydraulic press under 5 kN and circular disc of diameter ≈10 mm and thickness ≈2 mm were obtained. These circular discs were sintered at 1500 °C for 12 h in a muffle furnace and normally cooled to room temperature.

X-ray diffraction (XRD) patterns of the calcined powders and sintered pellets were recorded on X-ray diffractometer (Rigaku Miniflex II Desktop, Japan) in 2θ range from 20° to 80° and at a step size of 0.02°. For microstructural studies, the sintered pellets were polished using emery papers of various grades, followed by velvet cloth polishing using a diamond paste till mirror finish. The pellets were then washed with isopropanol several times to remove particles of SiC and diamond. Thereafter, the pellets were chemically etched to reveal the grains and grain boundaries and coated with Au (by Au sputtering). A field emission scanning electron microscope (Nova Nano SEM 450, USA) was used to record images of polished surfaces of the sintered pellets. For dielectric measurements, flat surfaces of the pellets were polished and high-temperature silver paste was applied, followed by heating at 700 °C for 10 min. Capacitance (C) and conductance (G) were measured in wide frequency and temperature ranges using an LCR meter (Agilent E-4980, USA).

III. Results and discussion

3.1. Phase evolution and crystal structure

To gain clear insight into sequences of the used solid-state reaction the mixture was calcined at different temperatures for 12 h. XRD pattern of the mixture obtained after each step of heat treatment was recorded and analysed. The X-ray diffraction (XRD) patterns of the powders after calcination at different temperatures along with the standard patterns of Sr_2MnO_4, Sr_2SnO_4 and $Sr_7Mn_4O_{15}$ are shown in Fig. 1a.

The XRD pattern of the powder calcined at 1200 °C (Fig. 1a) contains mainly peaks of Sr_2MnO_4 and intermediate $Sr_7Mn_4O_{15}$ phase. For the in-depth analysis, we have plotted the highest intensity peak of (103) plane on magnified scale and shown in the frame of Fig. 1a. Magnified view of the highest intensity peak (103) has revealed an asymmetry in the shape of the peak towards the lower angle side. The wideness and asym-

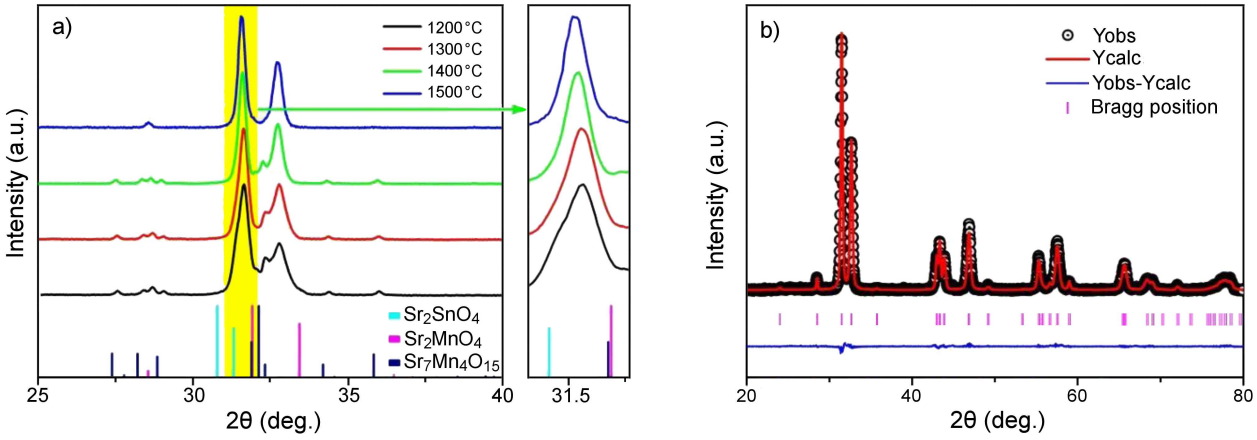

Figure 1. XRD of powders calcined at different temperatures (a) and Rietveld refinement of XRD pattern of powder calcined at 1500 °C (b)

metry of this peak indicate the presence of Sr_2SnO_4 phase in the calcined powder beside Sr_2MnO_4 and $Sr_7Mn_4O_{15}$ phases. It is reported that single-phase powder by solid state reaction method of Sr_2SnO_4 can be synthesized at 1200 °C whereas by the same method formation of the Sr_2MnO_4 phase is possible at ≥1500 °C [20,27]. The presence of Sr_2MnO_4 phase in powder calcined at 1200 °C indicates that Sr_2SnO_4 has acted as seed-particles and reduced the formation temperature of phase Sr_2MnO_4 (at 1200 °C) by the process of induced nucleation. It is not surprising because both Sr_2SnO_4 and Sr_2MnO_4 phases have tetragonal structure and space group $I4/mmm$ [20,27].

On increasing calcination temperature to 1300 °C no obvious change in XRD pattern was observed except reduction in asymmetry and shifting of the (103) peak towards the lower angle side. The peak corresponding to (103) plane was further moved towards lower angle side and became more symmetric after the increase in temperature to 1400 °C. In addition, it is observed that as calcination temperature increases height of the peaks (intensity) corresponding to $Sr_7Mn_4O_{15}$ phase decreases. The XRD pattern of the powder calcined at 1500 °C matches exactly with the standard XRD pattern of Sr_2MnO_4 phase. No peaks corresponding to impurity phase $Sr_7Mn_4O_{15}$ are present in the XRD pattern of the powder calcined at 1500 °C. On increasing calcination temperature, gradual shifting of position towards lower angle side and reduction in an asymmetry of (103) peak is strong evidence for the formation of solid solution between Sr_2SnO_4 and Sr_2MnO_4. The position of (103) peak in the XRD pattern of powder calcined at 1500 °C lies between the position of the same peak for the end members Sr_2SnO_4 and Sr_2MnO_4. The ionic radius of Sn^{4+} (0.69 Å) is slightly larger than the ionic radius of Mn^{4+} (0.53 Å). Thus, when Sn^{4+} replaces Mn^{4+} ion in Sr_2MnO_4 expansion of cell volume takes place (lattice parameters increase) and Bragg's angle decreases. The shifting of (103) peak towards lower angle side on increasing calcination temperature (1200 to 1500 °C) confirms the formation of solid solution $Sr_2Mn_{0.7}Sn_{0.3}O_4$. The Rietveld refinement of the XRD pattern of powder calcined at 1500 °C was carried out to determine structural parameters. In Fig. 1b experimentally recorded pattern, calculated XRD pattern and their difference are shown. The structural parameters along with reliability factors are presented in Table 1.

Table 1. Structural parameters and reliability factors obtained by the Retiveld refinement

Lattice/cell parameters	$a = b = 3.860$ Å, $c = 12.530$ Å
Cell volume	188.653 Å^3
Sr (4e)	(0,0,0.355)
Mn/Sn (2a)	(0,0,0)
O1 (4c)	(0,0.5,0)
O2 (4e)	(0,0,0.161)
Mn/Sn–O1	1.940 Å
Mn/Sn–O2	2.027 Å
Sr–O1	2.653 Å
Sr–O2	2.426 Å
Mn–O1/Mn–O2	0.96 Å
R_p	14.8
R_{wp}	10.8
R_{exp}	9.7
χ^2	1.99

3.2. Microstructural studies

SEM image of the pellet sintered at 1500 °C is shown in Fig. 2a. The micrograph exhibits well-defined grains of cuboidal shape and distribution in the grain size. A histogram of the distribution of grain size was obtained using the ImageJ software package. By fitting the Gaussian function to these histograms (Fig. 2b) average grain size of the sample was calculated to be 1.55 μm.

3.3. Negative dielectric behaviour

Variations of real (ε_r') and imaginary (ε_r'') components of the dielectric constant (ε_r) and dielectric loss ($\tan\delta$) with temperature at a few representative frequencies are shown in Figs. 3a, 3b and 3c, respectively. It is observed that as the temperature increases the value of

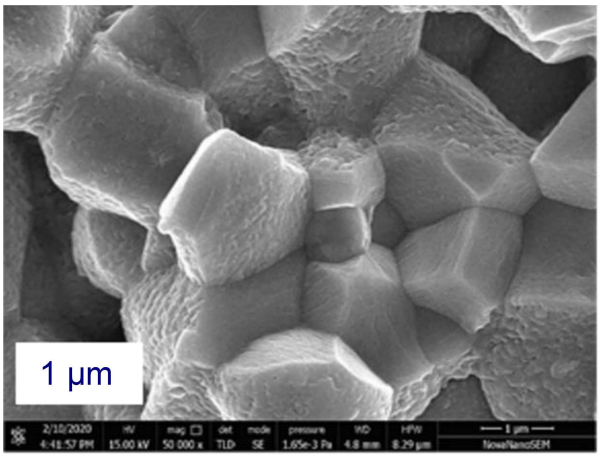

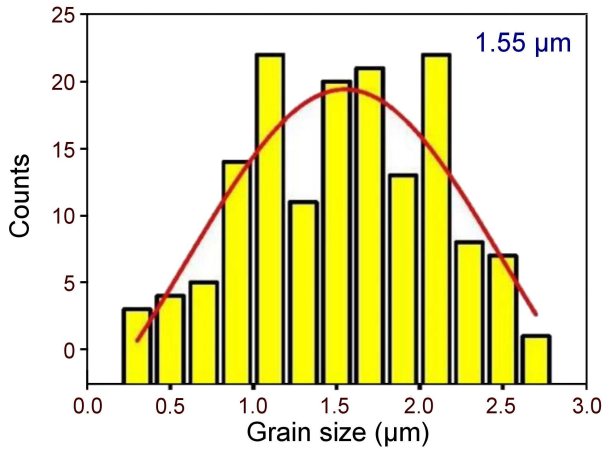

Figure 2. SEM image of the sintered pellet (a) and histograms showing the distribution of grain sizes in the sample (b)

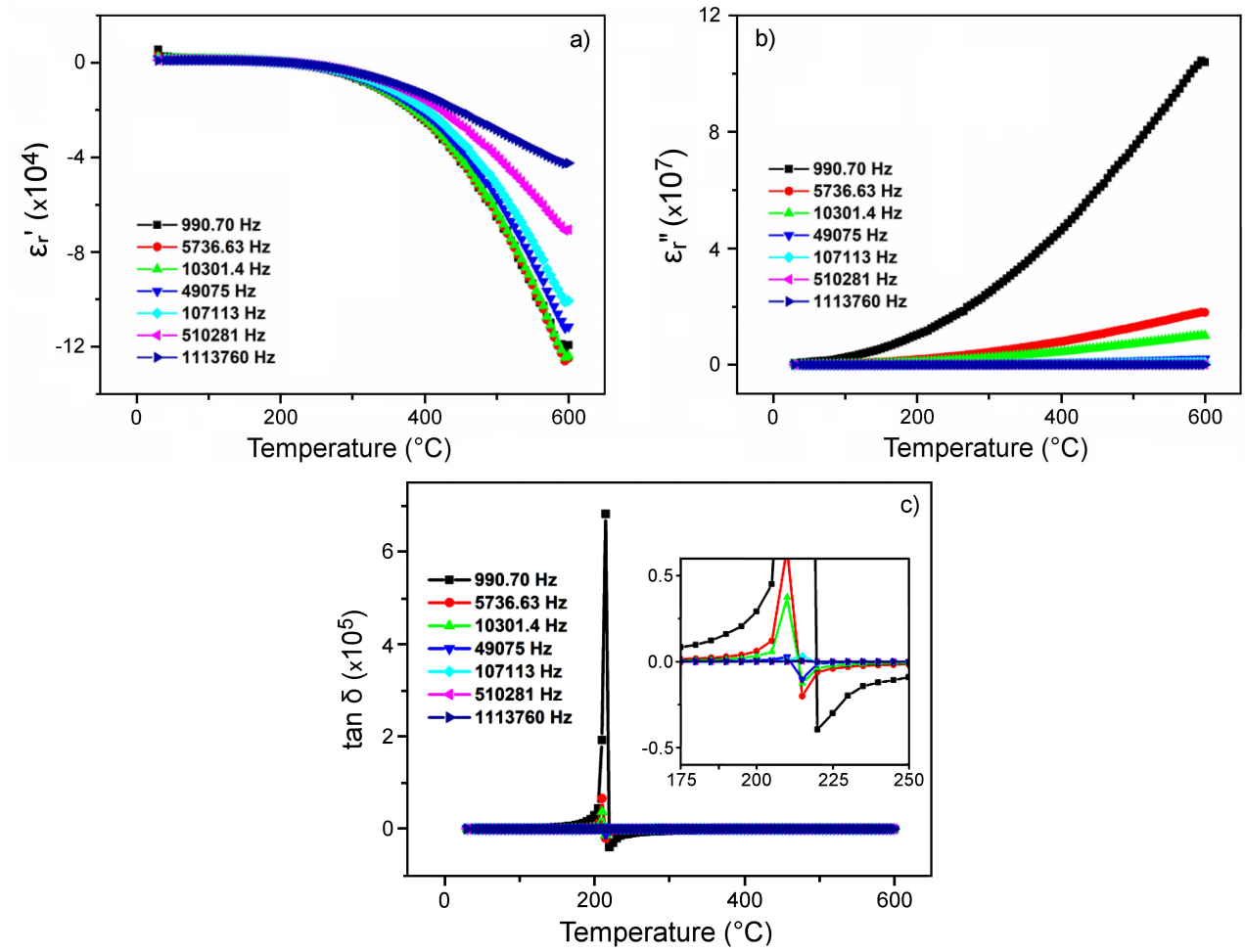

Figure 3. Variation of (a) real part of permittivity, ε_r', (b) imaginary part of permittivity, ε_r'' and (c) dissipation factor, $\tan\delta$ with the temperature at selected frequencies

ε_r' decreases and at a particular temperature (210 °C at 1 kHz) its value becomes negative. Further, it is noted that the temperature at and above which ε_r' attains negative values increases (approximately 210 °C) on increasing frequency from 1 kHz to 2 MHz.

Variation of the imaginary part of permittivity ε_r'' as a function of temperature at selected frequencies is shown in Fig. 3b. It is observed that ε_r'' increases continuously with the temperature at all the measured frequencies. The slope of the increment decreases with increasing frequency. However, its values remain positive at all measured frequencies and temperatures.

The plot of dissipation factor ($\tan\delta$) vs. temperature at a few repetitive frequencies is shown in Fig. 3c. Initially, $\tan\delta$ increases as temperature increases up to 210 °C, after that dielectric loss sharply drops to the lowest value (negative sign). On further increase in the temperature, values of $\tan\delta$ increase but remain negative up to the highest measured temperature, i.e. 600 °C. A similar trend was observed at all the frequencies, but the temperature at which resonance-like (sudden drop) behaviour is obtained slightly increases whereas the height of the resonance peak decreases with increasing frequency. At a given frequency, the temperature at which resonance in $\tan\delta$ vs. temperature plots is observed is the same at which ε_r' becomes negative (it is 210 °C at 10 kHz frequency). Decrease in the absolute value of $\tan\delta$ (magnitude of resonance on both sides) with increasing frequency is because $\varepsilon_r'' = \sigma_{DC}/\varepsilon_0 \cdot \omega$. At a given temperature σ_{DC} remains constant hence with increasing frequency ε_r'' decreases. Since $\tan\delta = \varepsilon_r''/\varepsilon_r'$, due to the decrease in the value of ε_r'', the value of $\tan\delta$ also decreases with increasing frequency.

Study of the negative permittivity behaviour of composites has become a hot topic for researchers. Composites have limitations when they are used in the form of coating/thin film or any other low dimension structures because of the presence of two components (ceramics and metals). Furthermore, a percolating conducting path is required for showing negative permittivity. Hence, for the use of negative permittivity materials in low dimension form efforts to discover and develop single-phase homogeneous materials showing negative permittivity are necessary. This task is challenging, but recently few single-phase ceramic oxides and polymers showing negative permittivity have been reported in the literature. Recently a review has been published on the negative epsilon materials [28]. For a comparative study, we have

Table 2. List of some single-phase ceramics showing negative permittivity and their parameters

Material	ε_r'	ε_r''	$\tan\delta$	Frequency	Temperature	Reference
$PrMnO_3$	-0.75×10^5	-	5×10^8	10 Hz	503 K	[17]
$La_{0.9}Sr_{0.1}MnO_3$	2×10^3	10^3	-	10 Hz	RT	[18]
$La_{0.8}Sr_{0.2}MnO_3$	0.5×10^5	10^4	-	10 Hz	RT	[18]
$La_{0.7}Sr_{0.3}MnO_3$	2.25×10^5	10^4	-	10 Hz	RT	[18]
$La_{0.6}Sr_{0.4}MnO_3$	-1.5×10^5	10^4	-	10 Hz	RT	[18]
$La_{0.5}Sr_{0.5}MnO_3$	-0.75×10^5	10^4	-	10 Hz	RT	[18]
$La_{0.5}Sr_{0.5}MnO_3$	-9×10^5	-	>10	10 Hz	90 °C	[28]
$La_{0.8}Sr_{0.2}MnO_3$	-2×10^3	-	-	1 MHz	-	[29]
$La_{0.5}Sr_{0.5}MnO_3$	-8×10^3	-	-	1 MHz	RT	[29]
$La_{0.7}Sr_{0.3}MnO_3$	-1.5×10^4	-	-	10 MHz	RT	[29]
$La_{0.8}Co_{0.16}Eu_{0.04}TiO_3$	−75	-	8×10^6	10 MHz	RT	[30]
TiN	-2×10^5	-	10^6	10 MHz	RT	[31]
$Sn_{0.94}Sb_{0.06}O_3$	-0.5×10^3	-	7×10^4	10 Hz	RT	[32]
$Sn_{0.92}Sb_{0.08}O_3$	-2.0×10^3	-	12×10^4	10 Hz	RT	[32]
$Sn_{0.9}Sb_{0.1}O_3$	-2.25×10^3	-	8×10^4	10 Hz	RT	[32]
$In_{1.82}Sn_{0.18}O_3$	-1×10^4	-	0.75×10^4	10 MHz	RT	[33]
$Bi_6Fe_{1.1}Mn_{0.9}Ti_3O_{18}$	-6×10^4	-	2500	1 kHz	520 K	[34]
$Bi_6Fe_{0.5}Mn_{1.5}Ti_3O_{18}$	-1×10^5	-	3000	1 kHz	433 K	[34]
$Bi_{0.3}Eu_{0.7}Sr_2CaCu_2O_{6.5}$	-1.5×10^5	-	10^5	1 Hz	433 K	[35]
Sr_2MnO_4	-2×10^3	-	-	1 kHz	600 °C	[22]
$LaFeO_3$	−400	600	-	0.8 GHz	RT	[36]
$La_{2-x}Sr_xNiO_4$	-1×10^5	2×10^5	-	500 kHz	300 K	[37]
$GdFeO_3$	−900	1500	-	1 GHz	RT	[38]
$Cu_{0.5}Ti_{0.5}Ba_2Ca_2(Cu_2Sn)O_{10-\delta}$	-1×10^7	2×10^7	−25	100 kHz	78 K	[39]
$La_{0.88}Ba_{0.12}CoO_3$	-5.5×10^4	15×10^5	-	100 kHz	RT	[40]
$Sr_2Mn_{0.7}Sn_{0.3}O_4$	-14×10^4	1×10^8	−0.7	1 kHz	600 °C	This work

presented dielectric parameters of the single-phase ceramic oxides which have exhibited negative permittivity behaviour in Table 2.

The negative values of the permittivity and dissipation factor in the measured frequency and temperature ranges of the composites have been attributed to a change in the electrical character of the sample, from capacitive to inductive one [41]. To confirm this observation for the sample $Sr_2Mn_{0.7}Sn_{0.3}O_4$, we have studied the real and imaginary parts of the impedance with frequency and the results are described in the next section.

3.4. Impedance and equivalent circuit analysis

Figures 4a and 4b show the variation of real (Z') and imaginary (Z'') parts of the impedance (Z^*) with angular frequency (ω) at a few representative temperatures. The real component of the impedance (Z') curve remains constant up to a particular frequency and above that it depends on ω at all temperatures. At temperatures ≤210 °C, Z' remains almost frequency independent up to a particular angular frequency (ω_H), and above ω_H, it starts decreasing with increasing frequency (Fig. 4a). The trend in Fig. 4a shows that the conduction is localized (via hopping mechanism). For temperatures >210 °C, Z' remains constant up to a certain frequency thereafter it starts increasing with increasing frequency. The increasing part of the Z' vs. ω plot at higher temperatures (>210 °C) indicates the metal-like conduction behaviour according to the skin effect. The decreasing value of Z' (plateau of the curves) with temperature indicates an increase in the value of DC conductivity (σ_{DC}) due to the generation of a large number of thermally activated charge carriers at high temperatures.

At a few selected temperatures, Z'' vs. ω plot is shown in Fig. 4b. At all temperatures up to a certain frequency Z'' remains constant. At temperatures ≤210 °C, as frequency increases the value of Z'' decreases sharply and attains the lowest negative value. On the other hand, at temperatures >210 °C, values of Z'' at all frequencies remain positive. As it is known for an alternating electric field, the change in the sign of Z'' from negative to positive with angular frequency (ω) can be attributed to the switching of the reactive elements from capacitive to inductive. We tried to fit experimental data by considering different equivalent circuits and found that the experimental results are in good agreement with data generated for the equivalent circuit shown in Fig. 4c. In Figs. 4a and 4b, the symbols are experimental data points and lines are theoretical curves for the equivalent circuit shown in Fig. 4c.

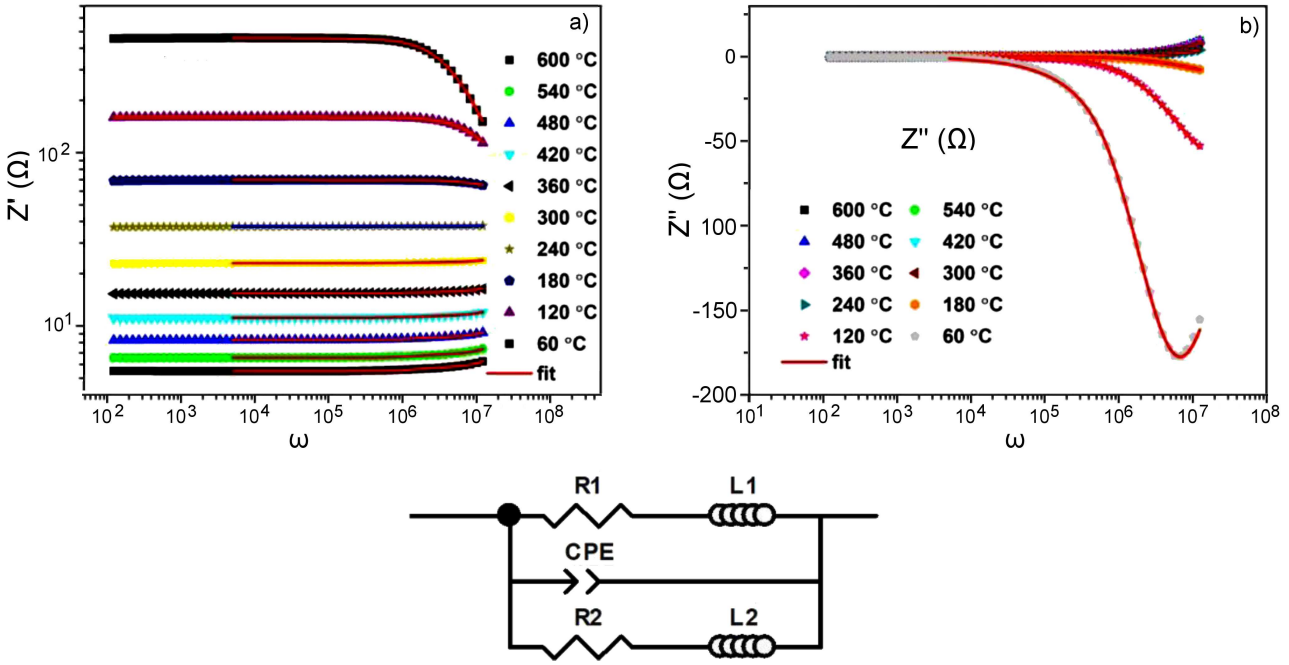

Figure 4. Variation of real part of impedance Z' (a), imaginary part of impedance Z'' (b) and equivalent circuit to fit experimental data (c)

It is discussed above that with increasing temperature Z'' changes its sign in the same manner as observed for ε'_r and $\tan\delta$. It is well documented in the literature that the permittivity of a material is strongly affected by the reactance. The change in sign of permittivity (positive to negative) is because of the change of the reactive element from capacitive to inductive nature. This result confirms that the negative permittivity can be credited to the dominance of the inductive element above a particular temperature (above 210 °C). The inductive characteristic of the sample is not surprising as transition metal Mn is present in the sample. The inductive nature of the reactive element may arise on account of time-varying electric field/electric current. Also, the observed resonance-like behaviour in $\tan\delta$ vs. temperature plots (Fig. 4c) is a consequence of changing the reactance from capacitive to inductive.

The presence of different components shown in the equivalent circuit (Fig. 4c) can be justified by correlating it with the composition of the sample. It is already mentioned that, in the sample, concentration of secondary phase $Sr_7Mn_4O_{15}$ decreases with increasing calcination temperature and disappears only when the powder is calcined at 1500 °C. Therefore, it is possible that the secondary phase $Sr_7Mn_4O_{15}$ was decomposed and grew on the surface of the desired phase $Sr_2Mn_{0.7}Sn_{0.3}O_4$, resulting in a compositional gradient. Particles of the synthesized sample may have two layers with different concentrations of Mn, Mn-rich and Mn deficient ($Sr_2Mn_{0.7}Sn_{0.3}O_4$). Herein, the Mn-rich region is assigned to the R_1 and L_1 (low resistive and inductive) elements while the Mn-deficient to R_2 and L_2 (high resistive inductive) elements. Constant phase element (*CPE*) is due to the pile up of the charge carriers at the interphase of these layers.

3.5. AC conductivity behaviour

Variations of σ_{AC} with $1000/T$ at a few selected frequencies are shown in Fig. 5. Effect of frequency on σ_{AC} conductivity is visible only at low temperatures (below 100 °C) and high temperatures (above 400 °C). It was observed that at low temperatures conductivity increases whereas at high temperatures it decreases with increasing frequency. This indicates a change in the electrical behaviour of the sample from semiconducting to metallic.

Variation of $\log\sigma_{AC}$ with $1000/T$ at intermediate temperatures is found to be linear at all frequencies. Lin-

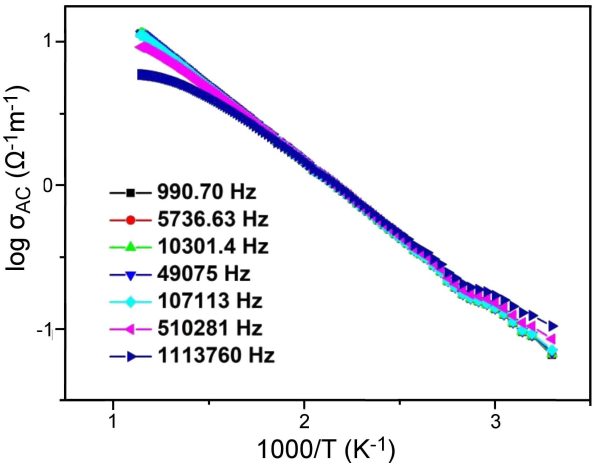

Figure 5. Variation of the logarithm of AC conductivity (σ_{AC}) with the inverse of temperature at few selected frequencies

ear behaviour in the intermediate temperature region indicates that σ_{AC} obeys the Arrhenius relation given by:

$$\sigma_{AC} = \sigma_0 \exp\left(-\frac{E_a}{k_B \cdot T}\right) \quad (1)$$

where, σ_0 is the pre-exponential factor, E_a is the activation energy, and k_B is the Boltzmann's constant. Activation energy is estimated by the linear fitting of the experimental data and its estimated value was 0.21 eV. The bandgap of Sr_2MnO_4 estimated experimentally using UV absorption data is 1.15 eV [20]. The calculated activation energy of electrical conduction (0.21 eV) is around $1/5^{th}$ (much lower) of the bandgap of material suggesting that the conduction in the synthesized sample is not due to the excitation of electrons from the valence band to the conduction band, but from the excitation of an electron from energy levels created due to defects.

IV. Conclusions

The reaction processes for the formation of $Sr_2Mn_{0.7}Sn_{0.3}O_4$ were investigated by calcining a mixture of the reactants between 1200–1500 °C using XRD. The reaction process for the formation of $Sr_2Mn_{0.7}Sn_{0.3}O_4$ has progressed in three stages: i) formation of Sr_2SnO_4, Sr_2MnO_4 and intermediate phase $Sr_7Mn_4O_{15}$, ii) inter mixing of Sr_2SnO_4 and Sr_2MnO_4 to form $Sr_2Mn_{0.7}Sn_{0.3}O_4$ and iii) decomposition of $Sr_7Mn_4O_{15}$ phase and dissolution into $Sr_2Mn_{0.7}Sn_{0.3}O_4$ phase. An equivalent circuit comprising two parallel *R-L* elements and one constant phase element (*CPE*) model fitted the impedance data very well. Analysis of the real and imaginary parts of the impedance (Z^*) has confirmed that negative permittivity and resonance in the tan δ vs. temperature plots at all frequencies are due to changes of the reactive element's nature from capacitive to inductive. The presence of more than two components in the equivalent circuit has confirmed compositional micro inhomogeneities in the synthesized sample. Negative permittivity and loss of the synthesized sample are comparable with other ceramic oxides showing negative permittivity. It is concluded that very few ceramic oxide systems have been investigated for negative dielectric behaviour.

Acknowledgments: The authors are grateful to the Head, Department of physics and the Co-ordinator, Central Instrument Facility Centre, IIT(BHU), Varanasi for providing experimental facilities.

References

1. C.H. Liu, N. Behdad, "High-power microwave filters and frequency selective surfaces exploiting electromagnetic wave tunneling through ε-negative layers", *J. Appl. Phys.*, **113** (2013) 064909.
2. Y. Li, N. Engheta, "Capacitor-inspired metamaterial inductors", *Phys. Rev. Appl.*, **10** (2018) 054021.
3. S. Sun, Z. Shi, L. Sun, L. Liang, D. Dastan, B. He, H. Wang, M. Huang, R. Fan, "Achieving concurrent high energy density and efficiency in all-polymer layered paraelectric/ferroelectric composites via introducing a moderate layer", *ACS Appl. Mater. Interfaces*, **13** (2021) 27522–27532.
4. L. Sun, Z. Shi, B. He, H. Wang, S. Liu, M. Huang, J. Shi, D. Dastan, H. Wang, "Asymmetric trilayer all-polymer dielectric composites with simultaneous high efficiency and high energy density: A novel design targeting advanced energy storage capacitors", *Adv. Funct. Mater.*, **31** (2021) 2100280.
5. M. Han, Z. Shi, W. Zhang, K. Zhang, H. Wang, D. Dastanc, R. Fan, "Significantly enhanced high permittivity and negative permittivity in $Ag/Al_2O_3/3D\text{-}BaTiO_3$/epoxy metacomposites with unique hierarchical heterogeneous", *Compos. Part A: Appl. Sci. Manuf.*, **149** (2021) 106559.
6. C. Liang , P. Song , H. Qiu , Y. Zhang , X. Ma , F. Qi , H. Gu, J. Kong, D. Cao, J. Gu "Constructing interconnected spherical hollow conductive networks in silver platelets/reduced graphene oxide foam/epoxy nanocomposites for superior, *Nanoscale*, **11** (2019) 22590–22598.
7. P. Song, B. Liu, H. Qiu, X. Shi, D. Cao, J. Gu, "MXenes for polymer matrix electromagnetic interference shielding composites: A review", *Compos. Commun.*, **24** (2021) 100653.
8. S. Ramadurgam, T.G. Lin, C. Yang, "Tailoring optical and plasmon resonances in core-shell and core-multishell nanowires for visible range negative refraction and plasmonic light harvesting: A review", *J. Mater. Sci. Technol.*, **31** (2015) 533–541.
9. A. Poddubny, I. Iorsh, P. Belov, Y. Kivshar, "Hyperbolic metamaterials", *Nat. Photonics*, **7** (2013) 958–967.
10. Z. Wang, K. Sun, P. Xie, Q. Hou, Y. Liu, Q. Gu, R. Fan, "Design and analysis of negative permittivity behaviors in barium titanate/nickel metacomposites", *Acta Mater.*, **185** (2020) 412–419.
11. G. Fan, Z. Wang, Z. Wei, Y. Liu, R. Fan, "Negative dielectric permittivity and high-frequency diamagnetic responses of percolated nickel/rutile cermets", *Compos. Part A Appl. Sci. Manuf.*, **139** (2020) 106132.
12. G. Fan, Z. Wang, H. Ren, Y. Liu, R. Fan, "Dielectric dispersion of copper/rutile cermets: dielectric resonance, relaxation, and plasma oscillation", *Scr. Mater.*, **190** (2021) 1–6.
13. K. Sun, J. Qin, Z. Wang, Y. An, X. Li, B. Dong, X. Wu, Z. Guo, R. Fan, "Polyvinyl alcohol/carbon fibers composites with tunable negative permittivity behavior", *Surfaces Interfaces*, **21** (2020) 100735.
14. K. Sun, J. Dong, Z. Wang, Z. Wang, G. Fan, Q. Hou, L. An, M. Dong, R. Fan, Z. Guo, "Tunable negative permittivity in flexible graphene/PDMS metacomposites", *J. Phys. Chem. C*, **123** (2019) 23635–23642.
15. Z. Wang, X. Li, L. Wang, Y. Li, J. Qin, P. Xie, Y. Qu, K. Sun, R. Fan, "Flexible multi-walled carbon nanotubes/ polydimethylsiloxane membranous composites toward high-permittivity performance", *Adv. Compos. Hybrid Mater.*, **3** (2020) 1–7.
16. Z. Wang, K. Sun, H. Wu, P. Xie, Z. Wang, X. Li, R. Fan, "Compressible sliver nanowires/polyurethane sponge metacomposites with weakly negative permittivity controlled by elastic deformation", *J. Mater. Sci.*, **55** (2020) 15481–15492.

17. S.K. Balu, N.P. Shanker, M. Manikandan, N. Aparnadevi, T. Mukilraj, P. Manimuthu, C. Venkateswaran, "Crossover to negative dielectric constant in perovskite $PrMnO_3$", *Phys. Status Solidi A*, **217** [17] (2020) 2000230.
18. K.L. Yan, R.H. Fan, M. Chen, K. Sun, L.W. Yin, H. Li, S.B. Pan, M.X. Yu, "Perovskite (La,Sr)MnO_3 with tunable electrical properties by the Sr-doping", *J. Alloys Compd.*, **628** (2015) 429–432.
19. D. Balz, K. Plieth, "Die Struktur des Kaliumnickelfluorids, K_2NiF_4", *Zeitschrift Elektrochem., Ber. Bunsengesellschaft Phys. Chem.*, **59** (1955) 545–551.
20. G. Nirala, D. Yadav, S. Upadhyay, "Thermally activated polaron tunnelling conduction mechanism in Sr_2MnO_4 synthesized by quenching in ambient atmosphere", *Phys. Scripta*, **96** (2021) 045811.
21. T. Chupakhina, N. Melnikova, O. Gyrdasova, "Synthesis, structural characteristics and dielectric properties of a new K_2NiF_4-type phase $Sr_2Mn_{0.5}Ti_{0.5}O_4$", *J. Alloys Compd.*, **670** (2016) 105–112.
22. S. Liping, H. Lihua, Z. Hui, L. Qiang, C. Pijolat, "La substituted Sr_2MnO_4 as a possible cathode material in SOFC", *J. Power Sources*, **179** (2008) 96–100.
23. D. Singh, A. Mahajan, , "Synthesis, magnetic and electric transport properties of mixed-valence manganites $La_{0.5+x}Sr_{1.5-x}Mn_{0.5}Cr_{0.5}O_4$ (x = 0.1, 0.2 and 0.3)", *J. Solid State Chem.*, **207** (2013) 126–131.
24. M.V. Sandoval, C. Pirovano, E. Capoen, R. Jooris, F. Porcher, P. Roussel, G.H. Gauthier, "In-depth study of the Ruddlesden-Popper $La_xSr_{2-x}MnO_{4\pm\delta}$ family as possible electrode materials for symmetrical SOFC", *Int. J. Hydrogen Ene.*, **42** (2017) 21930–21943.
25. G. Nirala, D. Yadav, T. Katheriya, S. Upadhyay, "Temperature dependent negative permittivity in solid solutions $Sr_2Mn_{1-x}Sn_xO_4$ (x = 0, 0.3, 0.5)", *J. Eur. Ceram. Soc.*, **42** (2022) 453–461.
26. G. Nirala, T. Katheriya, D. Yadav, S. Pandey, S. Upadhyay, "Effect of Nb doping on epsilon negative behaviour of Sr_2MnO_4", *J. Mater. Sci.*, **57** (2022) 15862–15875.
27. A.N. Grundy, B. Hallstedt, L.J. Gauckler, "Assessment of the La-Sr-Mn-O system", *Calphad*, **28** [2] (2004) 191–201.
28. G. Fan, K. Sun, Q. Hou, Z. Wang, Y. Liu, R. Fan, "Epsilon-negative media from the viewpoint of materials science", *EPJ Appl. Metamater.*, **8** (2021) 11.
29. K. Yan, L. Shen, R. Fan, N. Bao, "Tailoring the electromagnetic properties of perovskite $La_{0.7}Sr_{0.3}MnO_3$ ceramics by Co doping", *J. Mater. Sci.*, **56** (2021) 10183–10190.
30. N.S. Kumar, R.P. Suvarna, K.C.B. Naidu, "Negative dielectric behavior in tetragonal $La_{0.8}Co_{0.2-x}Eu_xTiO_3$ (x = 0.01–0.04) nanorods", *Mater. Charact.*, **166** (2020) 110425.
31. G. Fan, P. Xie, Z. Wang, Y. Qu, Z. Zhang, Y. Liu, R. Fan, "Tailorable radio-frequency negative permittivity of titanium nitride sintered with different oxidation pretreatments", *Ceram. Int.*, **43** (2017) 16980–16985.
32. G. Fan, Z. Wang, K. Sun, Y. Liu, R. Fan, "Doping-dependent negative dielectric permittivity realized in mono-phase antimony tin oxide ceramics", *J. Mater. Chem. C*, **8** (2020) 11610–11617.
33. G. Fan, Z. Wang, K. Sun, Y. Liu, R. Fan, "Doped ceramics of indium oxides for negative permittivity materials in MHz-kHz frequency regions", *J. Mater. Sci. Technol.*, **61** (2021) 125–131
34. J.A. Bartkowska, D. Bochenek, P. Niemiec, "Multiferroic Aurivillius-type $Bi_6Fe_{2-x}Mn_xTi_3O_{18}$ ($0 \leq x \leq 1.5$) ceramics with negative dielectric constant", *Appl. Phys. A: Mater. Sci. Process.*, **124** (2018) 832.
35. M. Kılıç, Z. G. Özdemir, Y. Karabul, Ö. Karataş, Ö.A. Çataltepe, "Negative real permittivity in $(Bi_{0.3}Eu_{0.7})Sr_2CaCu_2O_{6.5}$ ceramic", *Phys. B Condens. Matter*, **584** (2020) 412080.
36. Q. Li, G. Zhu, "Controlling negative permittivity and permeability behavior in $LaFeO_3$ through sintering temperature", *Ceram. Int.*, **47** (2021) 5244–5248
37. T.D. Thanh, N. Van Dang, L. Van Hong, T.L. Phan, S.C. Yu, "Dielectric resonance effect with negative permittivity in a $La_{1.5}Sr_{0.5}NiO_{4+\delta}$ ceramic", *J. Korean Phys. Soc.*, **65** (2014) 1663–1668.
38. Q. Li, J. Li, "Tunable double resonance with negative permittivity and permeability in $GdFeO_3$ material by sintering temperature", *J. Alloys Compd.*, **817** (2020) 152778.
39. M. Mumtaz, N.A. Khan, S. Khan, "Frequency dependent dielectric properties of $Cu_{0.5}Tl_{0.5}Ba_2Ca_2(Cu_{3-y}M_y)O_{10-\delta}$ superconductor", *J. Appl. Phys.*, **111** (2012) 13920.
40. Z. Wei, Z. Wang, C. Xu, G. Fan, X. Song, Y. Liu, R. Fan, "Defect-induced insulator-metal transition and negative permittivity in $La_{1-x}Ba_xCoO_3$ perovskite structure", *J. Mater. Sci. Technol.*, **112** (2022) 77–84.
41. Z. Wei, Z. Wang, G. Fan, C. Xu, G. Shi, G. Zhang, Y. Liu, R. Fan, "Low-frequency plasmonic state and negative permittivity in copper/titanium dioxide percolating composites", *Ceram. Int.*, **47** (2021) 2208–2213.